

## Potential erosion capacity of gravity currents created by changing initial conditions

Zordan, Jessica; Schleiss, Anton J.; Franca, Mario J.

**DOI**

[10.5194/esurf-7-377-2019](https://doi.org/10.5194/esurf-7-377-2019)

**Publication date**

2019

**Document Version**

Final published version

**Published in**

Earth Surface Dynamics

**Citation (APA)**

Zordan, J., Schleiss, A. J., & Franca, M. J. (2019). Potential erosion capacity of gravity currents created by changing initial conditions. *Earth Surface Dynamics*, 7(2), 377-391. <https://doi.org/10.5194/esurf-7-377-2019>

**Important note**

To cite this publication, please use the final published version (if applicable).  
Please check the document version above.

**Copyright**

Other than for strictly personal use, it is not permitted to download, forward or distribute the text or part of it, without the consent of the author(s) and/or copyright holder(s), unless the work is under an open content license such as Creative Commons.

**Takedown policy**

Please contact us and provide details if you believe this document breaches copyrights.  
We will remove access to the work immediately and investigate your claim.



# Potential erosion capacity of gravity currents created by changing initial conditions

Jessica Zordan<sup>1</sup>, Anton J. Schleiss<sup>1</sup>, and Mário J. Franca<sup>1,2</sup>

<sup>1</sup>Laboratory of Hydraulic Constructions (LCH), School of Architecture, Civil and Environmental Engineering, École Polytechnique Fédérale de Lausanne (EPFL), Lausanne, Switzerland

<sup>2</sup>Water Science and Engineering department, IHE Delft Institute for Water Education and Department of Hydraulic Engineering, Delft University of Technology, Delft, the Netherlands

**Correspondence:** Jessica Zordan (jessica.zordan@epfl.ch)

Received: 9 November 2017 – Discussion started: 22 November 2017

Revised: 29 March 2019 – Accepted: 13 April 2019 – Published: 26 April 2019

**Abstract.** We investigate to what extent the initial conditions (in terms of buoyancy and geometry) of saline gravity currents flowing over a horizontal bottom influence their runout and entrainment capacity. In particular, to what extent the effect of the introduction of an inclined channel reach, just upstream from the lock gate, influences the hydrodynamics of gravity currents and consequently its potential erosion capacity is still an open question. The investigation presented herein focuses on the unknown effects of an inclined lock on the geometry of the current, on the streamwise velocity, on bed shear stress, and on the mechanisms of entrainment and mass exchange. Gravity currents were reproduced in the laboratory through the lock-exchange technique, and systematic tests were performed with different initial densities, combined with five initial volumes of release on horizontal and sloped locks. The inclination of the upstream reach of the channel (the lock) was varied from 0 % to 16 %, while the lock length was reduced by up to 1/4 of the initial reference case. We observed that the shape of the current is modified due to the enhanced entrainment of ambient water, which is the region of the current in which this happens most. A counterintuitive relation between slope and mean streamwise velocity was found, supporting previous findings that hypothesized that gravity currents flowing down small slopes experience an initial acceleration followed by a deceleration. For the steepest slope tested, two opposite mechanisms of mass exchange are identified and discussed, i.e., the current entrainment of water from the upper surface due to the enhanced friction at the interface and the head feeding by a rear-fed current. The bed shear stress and the corresponding potential erosion capacity are discussed, giving insights into the geomorphological implications of natural gravity currents caused in different topographic settings.

## 1 Introduction

Gravity currents are common phenomena that may occur spontaneously in nature or triggered by human activities. These flows are created by differences in hydrostatic pressures at the surface of contact of two fluids that have different densities. Examples of gravity currents generated in the atmosphere are katabatic winds, which are created by temperature inhomogeneities that originate the density gradient. Avalanches of airborne snow and plumes of pyroclasts from volcanic eruptions are atmospheric flows wherein suspended particles play a major role in producing the density gradi-

ent. If suspended sediment produces the extra density, gravity currents are called turbidity currents. Turbidity currents have received major attention, since the sedimentation they induce due to the high amount of sediments they transport has important economic costs related to the loss of volume for water storage (Palmieri et al., 2001; Schleiss et al., 2016). Among gravity currents caused by human actions, the release of pollutants into rivers, oil spillage in the ocean and desalination plant outflows are of primary importance due to their negative environmental impacts.

Gravity currents have been the subject of research over the last decades. Simpson (1997), Kneller and Buckee (2000), Huppert (2006), and Ungarish (2009) present a comprehensive review of the early work on natural and experimentally reproduced gravity currents. Recently, Azpiroz-Zabala et al. (2017) provided a new model for the gravity current structure. They argued that real-world turbidity currents in submarine canyons are characterized by a so-called “frontal cell”, which is highly erosive and therefore able to be self-sustaining and to outrun the slower-moving body of the flow, creating a stretched current. Nevertheless, authors working on small-scale experimentally reproduced gravity currents agree on describing the shape of the gravity current as composed by an arising highly turbulent front, called the head, followed by, in some cases, a body and a tail. The difference between the two concepts mainly comes from the observation timeframe, which is of the order of hours for experimentally reproduced gravity currents, while it is of days for the observations that Azpiroz-Zabala et al. (2017) made in Congo Canyon.

Within the body, which can reach a quasi-steady state, a vertical structure can be distinguished. A gravity current presents two main interfaces at which exchanges occur: at the bottom, generally a solid boundary, and at the top, at the interface with the ambient fluid. These are active boundaries at which mass and momentum exchanges are promoted (Ancy, 2012). Ambient fluid is entrained due to shear and buoyancy instabilities at the upper interface (Cantero et al., 2008), resulting in the dilution of the underlying current and modification of the density profile that characterizes a gravity current under stable density stratification (Turner, 1973). If the gravity current travels above an erodible bed, entrainment of material from the bottom can take place, which is conveyed with the current and sometimes redeposited at large distances from the original position (Zordan et al., 2018a). High shear stress associated with intense ejection and burst events influences erosion and bed load transport (Niño and Garcia, 1996; Cantero et al., 2008; Zordan et al., 2018a). For example, in the shallow shelf region of the lake it is frequently observed that cold water, which is relatively denser than that in open waters, starts to descend down the slope as a cold gravity current (Fer et al., 2002). The plume is able to transport suspended sediment together with the dissolved components, oxygen and pollutants into deeper water. A proper parameterization of both upper-layer and bottom entrainment is still an open research field that needs to be addressed. Indeed, small variations in entrainment highly influence flow dynamics (Traer et al., 2012).

Due to instabilities at the interface with the ambient fluid, the current entrains the lighter fluid and therefore it dilutes. Lock volume and lock slope are initial trigger conditions of experimentally reproduced gravity currents, and the main objective of the paper is to understand their influence on the transport capacity of the flows. We show how shear stress at

the boundaries is dependent on the conditions under which a gravity current forms, i.e., its initial and boundary conditions. Different initial conditions, representing configurations that can possibly be found in nature, are tested by varying the initial volume of denser fluid and the lock geometry.

Gravity currents are reproduced here in the laboratory by the lock-exchange technique. Three initial densities are tested in combination with five lock lengths on a horizontal bottom and with four inclinations of the upstream channel reach. The bottom of the channel was designed in order to have a variable slope angle of the lock and a following flat surface. We were in search of a threshold at which an inversion of the leading forces of these currents would occur, which are gravitational forces and friction at the upper interface with the ambient fluid. Previous studies mainly focused separately on either low slopes or large slopes, missing the analysis of the transition that is tested here thanks to a specific experimental setup that allows for a wider range of configurations. Finally, we use a parameter previously defined in Zordan et al. (2018a) for the evaluation of the bottom erosion capacity as a surrogate to evaluate the influence of each different trigger condition on the erosion capacity of the currents.

Britter and Linden (1980) reproduced gravity currents down a slope with no breaks and found a critical angle, which is typically less than a degree, over which buoyancy force is large enough to counteract the bottom friction, producing a steady flow. At larger slopes, two mechanisms affect the evolution of the current: the current entrains water from the upper surface due to the enhanced shear stress, and the head is fed by the rear steady current. Mulder and Alexander (2001) studied slope-break deposits created by turbidity currents. They said that the amount of mixing between flow and ambient fluid is influenced by slope changes, which furthermore cause significant changes in turbidite thickness. In the present study the effect of a change in slope is analyzed by testing a range of lock slopes below 16% ( $0^\circ \leq \alpha < 9^\circ$ ). It is expected that the two mechanisms mentioned by Britter and Linden (1980) will take place in the lock for the depletion current formed here due to the incremental gravitational forces, so a transition occurs from a friction-governed flow to a flow in which gravitational forces become more and more important. The erosion potential of a gravity current formed under such varying initial conditions is then discussed.

The present paper is structured as follows: first, the experimental setup and the process that allows for the noise reduction of the velocity measurements are described. Then, the results are presented: a method for the identification of the shape of the current is described and, by means of the mean streamwise velocity field, both bottom and interface shear stresses are computed. The variation in the shape caused by changing initial conditions (i.e., with different initial buoyancies, various lock lengths and lock-bottom inclinations) is therefore discussed. The potential water entrainment and bottom erosion capacity are estimated on the basis of the com-

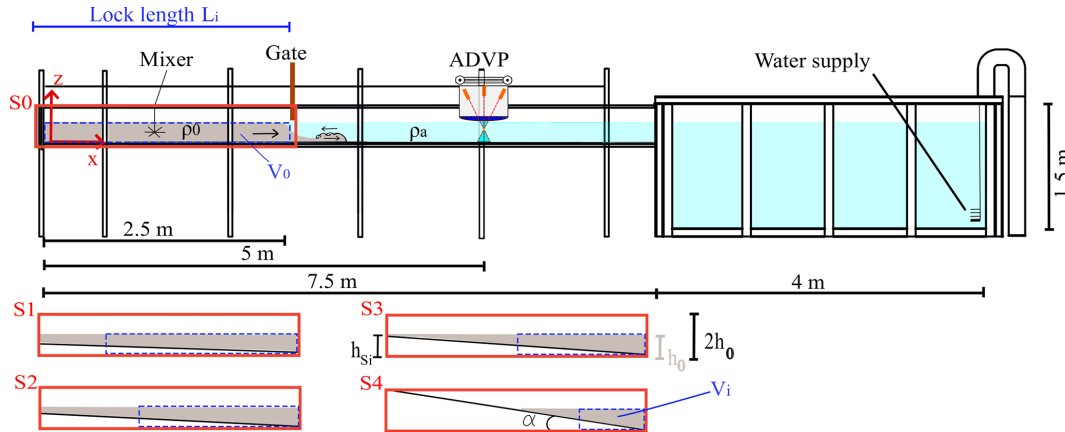


Figure 1. Longitudinal view and cross section of the experimental setup showing tested slope configurations S0 to S4 of lock volumes  $V_i$ .

puted shear stresses evolutions. Finally, an overview of the main findings is presented in the conclusions.

## 2 Methodology

### 2.1 Experimental setup

The tests are performed in a channel with a rectangular section 7.5 m long and 0.275 m wide. The gravity currents are reproduced through the lock-exchange technique by the sudden release of a gate that divides the flume in two parts whereby the fluids of different densities are at rest. Three buoyancy differences are tested in combination with five lock slopes ranging from  $S = 0\%$  (horizontal bed) to  $S = 16\%$  (tests S0 to S4). Figure 1 shows the configurations from a horizontal bed (S0) to the steepest slope (S4). By introducing a slope on the channel lock reach, the volume of denser fluid is reduced. This lock contraction is also tested separately by performing reference tests with the combination of the three initial densities and the five lock lengths that correspond to the very same volumes in the lock of the tests under inclined conditions. The experimental parameters are reported in Table 1.  $R_i-S_i$  refers to gravity currents reproduced by different initial densities with the presence of a lock slope, while  $R_i-L_i$  indicates the tests with varying initial density and lock length.

The channel is filled with 0.2 m of ambient water in one side and salty water, up to the same level, in the lock reach. Once the gate is removed, the saline current forms. At 2.5 m from the gate an acoustic Doppler velocity profiler (ADVP) is placed to measure 3-D instantaneous velocities along a vertical. The ADVP (Lemmin and Rolland, 1997; Hurther and Lemmin, 2001; Franca and Lemmin, 2006) is a nonintrusive sonar instrument that measures instantaneous velocity profiles using the Doppler effect without the need for calibration and was used with an acquisition frequency of 31.25 Hz. The velocity profiles are collected in time along a fixed vertical. The flume is connected to a final big reservoir that allows the current to dissipate and avoids its reflection upstream.

Normalization of the time is made using the scale  $t^* = h_b/u_b$ , where  $h_b$  is a vertical geometric scale, considered here as one-third of the total height of the fluid in the experimental tank,  $h_0$  ( $h_b = h_0/3$  and  $h_0 = 0.2$  m) and  $u_b = \sqrt{g'h_b}$  is the buoyancy velocity.

### 2.2 Data filtering

By means of an analysis of the power spectra of the raw data collected with the ADVP, noisy frequencies were mainly detected below 8 Hz. The instantaneous measurements were thus low-pass filtered with 8 Hz as a cutoff frequency (Zordan et al., 2018a). The 8 Hz cutoff has been chosen because the signal, for frequencies higher than 8 Hz, showed white noise. Time series of the mean streamwise and vertical velocities ( $\bar{u}$  and  $\bar{w}$ ) for the unsteady gravity current were derived after a filtering procedure that consisted of the application of a moving average over a time window that is chosen through the analysis of the power spectra distribution as in Baas et al. (2005). This analysis showed that for a time window of 0.32 s, the harmonics of all the meaningful frequencies were still recognizable, while by increasing the time window, the harmonics of progressively smaller frequencies gradually lose power and become impossible to distinguish (Baas et al., 2005). Thus, this window length was chosen for the moving average defining  $\bar{u}$  and  $\bar{w}$ . The turbulent fluctuation time series ( $u'$  and  $w'$ ) is then calculated using the Reynolds decomposition:

$$u = \bar{u} + u', \tag{1}$$

where  $u$  is the instantaneous velocity. The cleaning procedure with the velocity signals and corresponding spectra is shown in Fig. 2.

**Table 1.** Experimental parameters.  $\rho_0$  is the initial density of the mixture in the upstream tank (measured with a densimeter),  $g'$  is the reduced gravity corresponding to  $\rho_0$ ,  $Re_0 = u_0 h_0 / \nu_c$  is the Reynolds number based on initial quantities with  $u_0 = \sqrt{g' h_0}$  the initial buoyancy velocity,  $h_0 = 0.2$  m is the total height of the water column,  $\nu_c$  is the kinematic viscosity of the denser fluid,  $\alpha$  is the angle of inclination of the bottom in the lock,  $S$  is the lock slope expressed in percentage ( $h_{S_i} / L_0$ , with  $h_{S_i}$  the height as in Fig. 1),  $L_i$  is the length of the upstream lock reach and  $V_i / V_0$  is the percentage of volume of the upstream lock reach with respect to the configuration  $L_0$ .

$S_i$ tests	$\rho_0$ ( $\text{kg m}^{-3}$ )	$g'_0$ ( $\text{m}^2 \text{s}^{-1}$ )	$u_0$ ( $\text{m s}^{-1}$ )	$Re_0$ (–)	$S$ (%)	$\alpha$ (°)	$V_i / V_0$
R1.S0	1028	0.29	0.24	48166	0	0.00	1.000
R1.S1	1028	0.29	0.24	48166	4	2.29	0.750
R1.S2	1028	0.29	0.24	48166	6	3.43	0.625
R1.S3	1028	0.29	0.24	48166	8	4.57	0.500
R1.S4	1028	0.29	0.24	48166	16	9.09	0.250
R2.S0	1038	0.39	0.28	55857	0	0.00	1.000
R2.S1	1038	0.39	0.28	55857	4	2.29	0.750
R2.S2	1038	0.39	0.28	55857	6	3.43	0.625
R2.S3	1038	0.39	0.28	55857	8	4.57	0.500
R2.S4	1038	0.39	0.28	55857	16	9.09	0.250
R3.S0	1048	0.49	0.31	62610	0	0.00	1.000
R3.S1	1048	0.49	0.31	62610	4	2.29	0.750
R3.S2	1048	0.49	0.31	62610	6	3.43	0.625
R3.S3	1048	0.49	0.31	62610	8	4.57	0.500
R3.S4	1048	0.49	0.31	62610	16	9.09	0.250
$L_i$ tests	$\rho_0$ ( $\text{kg m}^{-3}$ )	$g'_0$ ( $\text{m}^2 \text{s}^{-1}$ )	$u_0$ ( $\text{m s}^{-1}$ )	$Re_0$ (–)	$L$ (m)	$V_i / V_0$ (–)	
R1.L0	1028	0.29	0.24	48166	2.500	1.000	
R1.L1	1028	0.29	0.24	48166	1.875	0.750	
R1.L2	1028	0.29	0.24	48166	1.563	0.625	
R1.L3	1028	0.29	0.24	48166	1.250	0.500	
R1.L4	1028	0.29	0.24	48166	0.625	0.250	
R2.L0	1038	0.39	0.28	55857	2.500	1.000	
R2.L1	1038	0.39	0.28	55857	1.875	0.750	
R2.L2	1038	0.39	0.28	55857	1.563	0.625	
R2.L3	1038	0.39	0.28	55857	1.250	0.500	
R2.L4	1038	0.39	0.28	55857	0.625	0.250	
R3.L0	1048	0.49	0.31	62610	2.500	1.000	
R3.L1	1048	0.49	0.31	62610	1.875	0.750	
R3.L2	1048	0.49	0.31	62610	1.563	0.625	
R3.L3	1048	0.49	0.31	62610	1.250	0.500	
R3.L4	1048	0.49	0.31	62610	0.625	0.250	

### 3 Results

#### 3.1 The shape of the current

A criterion to identify the two main regions of a gravity current, the head and the body, is established here. Inspired by Nogueira et al. (2014), who considered the product of the depth-averaged streamwise velocity with the depth-averaged density of the current, we decide to adopt a similar procedure but taking into account the velocity field and the shape as relevant characteristics for distinguishing between the head and

body. These distinctive features (a characteristic velocity and the contour of the current) have therefore been used in order to define a function that allows us to universally identify those regions of the currents. The kinematic function ( $H$ ) is computed as the product between the instantaneous depth-averaged streamwise velocity,  $u_d(t)$ ,

$$u_d(t) = \frac{1}{h} \int_0^h u(z, t) dz, \quad (2)$$

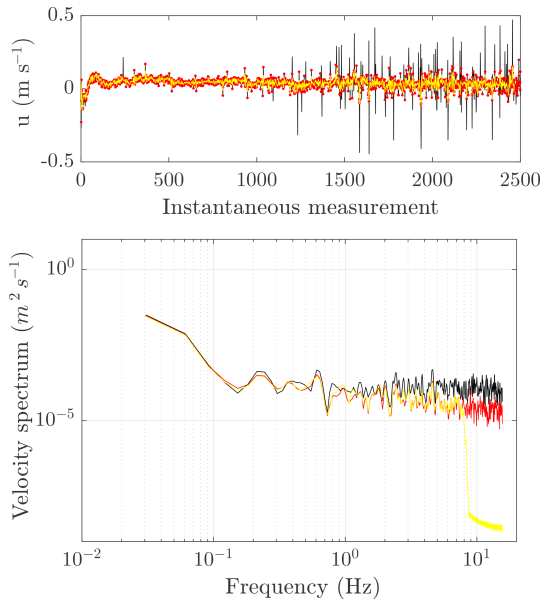


**Figure 2.** Raw velocity data (black) and despiked data (red) obtained with the procedure proposed by Goring and Nikora (2002). Then, through the analysis of the velocity spectra (bottom), the cut-off frequency of 8 Hz has been identified in order to low-pass filter the noisy frequencies (yellow line).

and the current height,  $h(t)$ , that is identified here by the position at which the streamwise velocity is equal to zero, as in Zordan et al. (2018a).  $H$  is thus defined as

$$H(t) = u_d(t)h(t). \tag{3}$$

By dimensional analysis, the function  $H$  corresponds to a flow rate per unit width. The head of the gravity current is characterized by a high specific flow rate that decreases at the rear of the head, a region in which fluid is recirculated through vortical movements.

Here,  $L_h$  identifies the temporal extension of the head and it is identified by the first meaningful local minimum of the function  $H$ , starting from the front. The conversion from time to length scale may be done by using the Taylor frozen hypothesis and considering a reference velocity of the current velocity as advection velocity. This method is coherent for all the experiments performed, and the value of the  $H$  function is shown in Fig. 3.

The body length is analyzed by using the cumulative sum of the function  $H$ . This is a region in which a quasi-steady regime is established for a certain time length. This implies that  $\sum H$  shows a linear increment in time. The limit of the body is therefore defined by analyzing the linear evolution that is fitted by a linear regression with a least squares method for progressively longer portions of the accumulated summed data. The analysis of the development of the  $R^2$  value, the coefficient of determination, allows us to find the extension of the linear portion that corresponds to the temporal extent

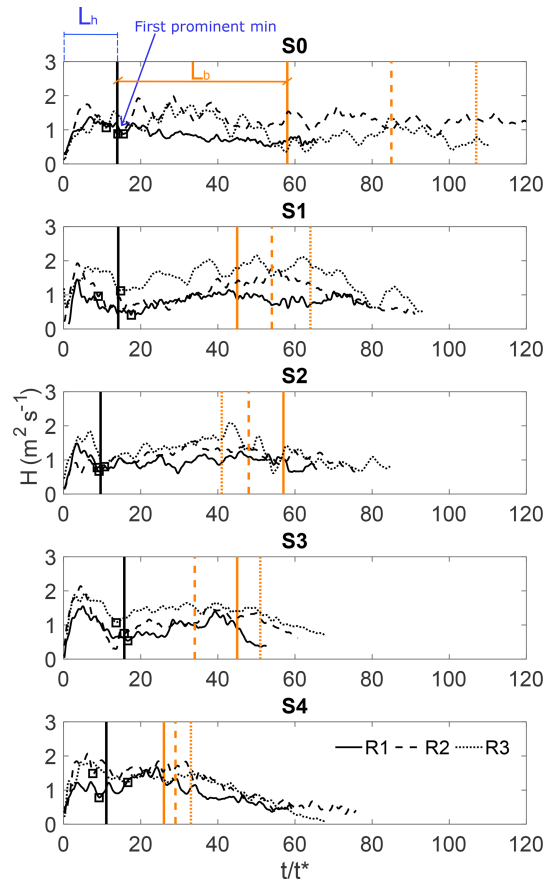


**Figure 3.** Determination of the gravity current head extension from the first prominent minimum of the function  $H$  ( $L_h$ ). The extension of the body ( $L_b$ ), as identified by the cumulative sum of the depth-averaged streamwise velocity, is also traced with the red vertical lines.

of the body region ( $L_b$ ).  $R^2$  is defined as the square of the correlation between the response values and the predicted response values. It is computed as the ratio of the sum of squares of the regression (SSR) and the total sum of squares (TSS) as

$$R^2 = \frac{SSR}{TSS} = \frac{\sum_{i=1}^n (y_i - \hat{y}_i)^2}{\sum_{i=1}^n (y_i - \bar{y})^2}, \tag{4}$$

where  $\bar{y}$  is the average of the response  $y$ ,  $\hat{y}$  is the regression line and  $n$  the number of observations  $i$ . In Fig. 3 the development of the function  $H$  is shown for the tests with the lock slope.

The same procedure is adopted for tests  $R_i.L_i$ , and the results can be found in Zordan et al. (2018b).

The form of the currents was identified by the zero streamwise velocity contour. In Fig. 4 the contours of each test with the lock slope are compared with the correspondent refer-

ence test with lock-length variation. The results are grouped by the initial density on the lock (columns in the figure) and by pairs of tests with the same volume of the lock but for different slopes. The extension of the head and body as identified by previous methods is also reported with the vertical lines. Dashed lines refer to tests  $S_i$ , while continuous lines correspond to  $L_i$  tests.

In Fig. 4 we can see that the head of the currents does not show any relevant change. Instead, the extension of the body is affected: it is reduced with an increasing inclination of the upstream channel reach and the same goes for tests produced by reduced lock volume. A dependency on the initial density is noticed, and three out of the total five slopes lead to the formation of a longer body with greater initial buoyancy. This can be verified in Fig. 3 where extensions of the bodies are plotted with the vertical orange lines. R1, R2 and R3 produce progressively longer bodies for tests S0, S1 and S4.

The largest deviation between the two contours of corresponding tests  $L_i-S_i$  is noticed for the last configuration, with the  $R_i-L4$  tests showing a shorter body and a more defined tail, while for the correspondent tests with the inclined lock the body is more extended.

### 3.2 Mean velocity field

In Fig. 5 the mean streamwise velocity field on the background and velocity vectors of the components ( $\bar{u}$ ,  $\bar{w}$ ) are shown for all the tests performed. The heads of the currents are indicated by the vertical dashed lines, and the zero streamwise velocity contours are marked by the black lines. We can notice that the structures of the currents are quite similar in all configurations. An arising head is followed by a zone of high mixing, characterized by the presence of billows (due to Kelvin–Helmholtz types of instabilities; Simpson, 1972) that are due to shear at the rear part of the elevated head. The body and tail are not always well-defined regions, mainly for the class of tests down an incline, and therefore the contour is not drawn. Moreover, tests  $S_i$  show lower streamwise velocities within the head and body with respect to correspondent  $L_i$  tests.

By comparing tests  $S_i$  with the correspondent  $L_i$  tests, which have the same lock volume but are performed without upstream slope, it is noticed that mean streamwise velocity is slightly higher for tests on a horizontal bed. This can appear to some extent contradictory, but that behavior has already been mentioned in the literature in the study of Beghin et al. (1981), who were among the first to investigate the role of the slope on the physics of a gravity current. They showed that test flows on small slopes, for tests in which the entire channel was inclined (typically less than  $5^\circ$ ), experience a first acceleration phase followed by a deceleration phase. This is because of the fact that, although the gravitational force increases as the lock slope becomes more inclined, there is also increased entrainment, both into the head itself and into the

flow behind. This produces an extra dilution of the current with a decrease in buoyancy.

### 3.3 Bottom and upper shear stress

The sedimentological impact of a gravity current is the result of the complex hydrodynamics of this flow. Sediment entrainment is a complex mechanism mainly due to the difficulty in defining the fluctuating nature of turbulent flow (Salim et al., 2017). In Zordan et al. (2018a) the transport of sediment within a gravity current is linked to bed shear stress, which is considered here to be a “surrogate” measure of it. The fact that bed shear stress is affected by the changing initial conditions of the current thus explains how the entrainment capacity of a current is altered. Bed shear stress temporal evolution is calculated by following the procedure in Zordan et al. (2018a) in which it was assumed that the mean flow met the conditions necessary for the fitting of the overlapping layer by the logarithmic law of the wall as (Ferreira et al., 2012)

$$\frac{\bar{u}(z)}{u_*} = \frac{1}{k} \ln \frac{z}{z_0}, \quad (5)$$

where  $\bar{u}(z)$  is the mean velocity,  $u_*$  is the friction velocity, which is the velocity scale corresponding to the bed shear stress (Chassaing, 2010),  $k$  is the von Kármán constant,  $z$  is the vertical coordinate and  $z_0$  is the zero velocity level.

The equation of the logarithmic law of the wall can be rewritten as

$$u = A \ln(z) - B, \quad (6)$$

where

$$A = \frac{u_*}{k}, \quad B = \frac{u_*}{k} \ln(z_0). \quad (7)$$

Then, by determining the coefficients  $A$  and  $B$  through a fitting procedure, one obtains an estimation of  $u_*$ , which is the velocity scale corresponding to the bed shear stress.

Bed shear stress is afterwards computed by considering a constant initial density that is equal here to the initial density in the lock ( $\rho_0$ ):

$$\tau_b = \rho_0 u_*^2. \quad (8)$$

The fitting procedure of the bottom logarithmic layer was determined stepwise by extending a linear least squares fitting range (in a semilogarithmic scale) from the lowest measured point until the point along the vertical of maximum streamwise velocity. Then, within this region, the sublayer that provided the best regression coefficient was chosen and considered for the estimation of  $u_*$ , corresponding to the extent of the logarithmic layer as was shown in Zordan et al. (2016).

The flow boundary is assumed to be smooth by verifying that the shear Reynolds number (or skin roughness,  $k_s$ ,

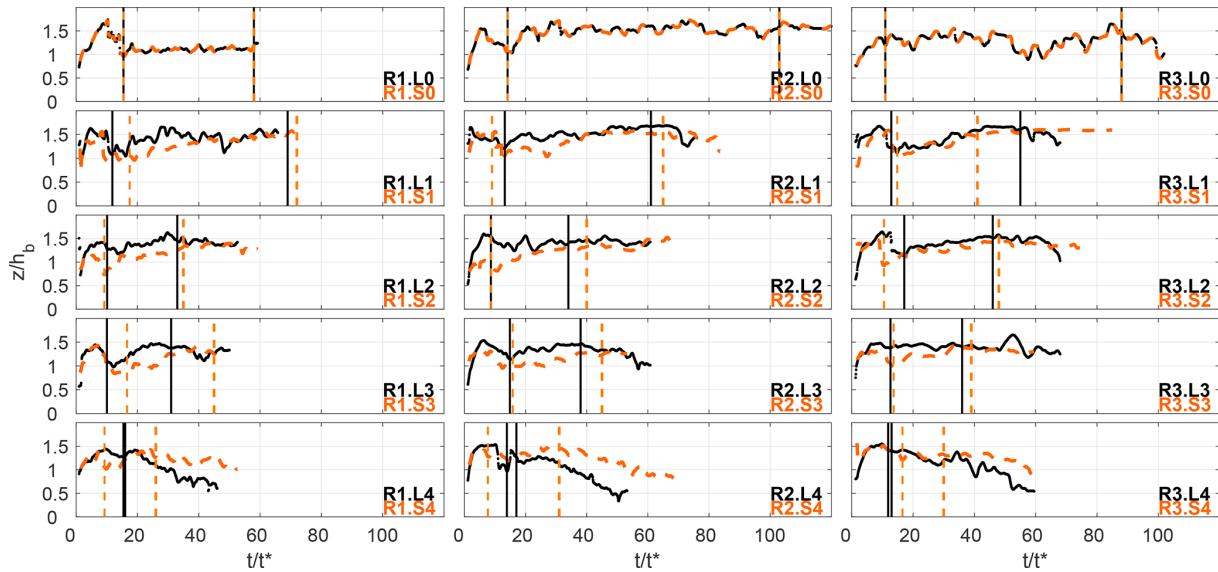


**Figure 4.** Gravity current contours, as identified by the zero streamwise velocity contour, for tests with the lock slope and correspondent tests with lock-length variation.

normalized by the viscous layer) is less than 5 (Nezu et al., 1994):

$$\frac{k_s u_*}{\nu} \leq 5. \tag{9}$$

The classic value of the von Kármán constant of  $k = 0.405$  is adopted. A discussion of the estimation of  $k$  can be found in Ferreira (2015).

The bed shear stress time evolution of gravity currents with lock slope ( $\tau_{b,S}$ ) is compared to the analogous results for tests with decreasing lock ( $\tau_{b,L}$ ). Therefore, the time-averaged bed shear stress has been computed and the ratio  $\overline{\tau_{b,L}}/\overline{\tau_{b,S}}$  is shown in Fig. 6. Tests performed with a lock slope show on average lower values of bed shear stress ( $\overline{\tau_{b,L}}/\overline{\tau_{b,S}} \geq 1$ ). By increasing the lock slope this tendency is less evident and the mean bed shear stress is comparable for both conditions with varying lock slope and with different lock lengths. Moreover, tests performed with the highest density difference seem less affected by a changing configuration ( $S_i L_i$  with  $i = 1, 2, 3, 4$ ). The detailed time series for this condition are presented in Fig. 8, where we can see that from normalized time  $t/t^* \simeq 20$ , i.e., in the body region, bed shear stress is slightly higher for tests  $S_i$  than in the correspondent  $L_i$  tests.

At the upper boundary of the gravity currents, i.e., the interface with the ambient water, studies on turbulent flow near a density interface confirmed that under certain conditions, the turbulent boundary layer theory can be applied as well (Lofquist, 1960; Csanady, 1978) and that the “law of the wall” can be used to estimate the shear stress here. By hypothesizing a constant mean value of water viscosity and hydraulically smooth conditions, the estimation of an interface shear stress ( $\tau_m$ ) is made; qualitatively, the estimation

that will result is enough for the purpose of the present study. The time evolution of interface shear stress is therefore computed following the same procedure as for the bottom shear stress. In this case the fitting procedure of the logarithmic layer is determined by considering the mixing layer as defined in Zordan et al. (2018b). This layer is delimited at the top by the zero streamwise velocity contour and at the bottom by the height of the current as defined by the Turner’s integral scales (Ellison and Turner, 1959). Within this layer, the (at least three) consecutive measurement points along the velocity profile that were giving the highest  $R^2$  were considered for fitting. The time average of the interface shear stress is compared by means of the ratio  $\overline{\tau_{m,L}}/\overline{\tau_{m,S}}$  (Fig. 7), showing that in general tests performed with varying lock lengths present higher values with respect to correspondent tests with lock-slope variation, i.e.,  $\overline{\tau_{m,L}}/\overline{\tau_{m,S}} \geq 1$ .

Again, the main differences between tests with reduced lock and respective tests with lock slope are for the fourth configuration, detailed time series of which are shown in Fig. 9. The steepest slopes present higher values of interface shear stress in the body region with respect to the correspondent tests with the same initial volume of release but flowing on a horizontal bed.

## 4 Discussion

### 4.1 Shape variation of gravity current with the lock slope

The extensions of the body of correspondent tests performed with the lock slope or with a horizontal bed and with varying lock lengths are compared in Fig. 10. For lower lock slopes the body extension is similar to the currents produced with the same lock volume but with a horizontal bottom. How-



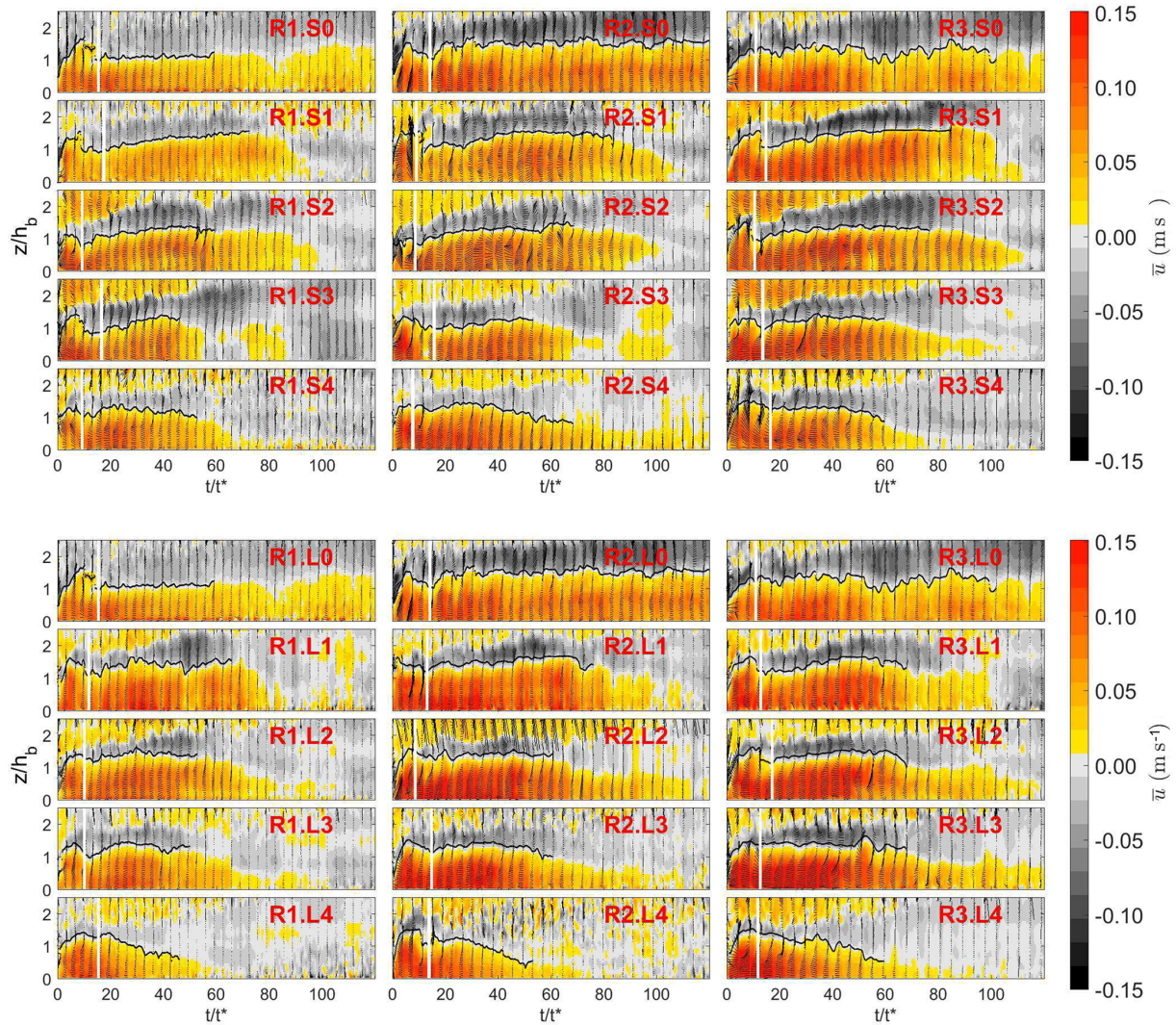


**Figure 5.** Streamwise velocity field on the background and velocity vectors of the components ( $u$ ,  $w$ ). The head of the current is delimited by the vertical white line. The contour of the current is indicated in black.

ever, for lock slopes at 16%, the body region for tests  $S_i$  is longer than correspondent tests  $L_i$ . At this point two mechanisms affect the evolution of the current: the current entrains water from the upper surface due to the enhanced friction at the interface between the denser flow and the counter-current progressively advancing upwards the lock, and the head is fed by the rear current. The flow of tests S4 show that the characteristics of the upstream flow in the lock are influencing the flow even when the current reaches the measuring point: (i) an extended body is the result of water entrainment at the upper surface of the current that creates dilution and expansion of the fluid in the current; and (ii) the fluid in the body becomes faster as a result of the gravitational forces as in Britter and Linden (1980) (Fig. 5). Britter and Linden (1980) showed that for currents flowing along a horizontal boundary, the head is the controlling feature. However, down a slope, the body becomes more determinant in the gravity

current evolution since it is up to 30%–40% faster than the head velocity, depending on the slope, therefore being able to move faster fluid into the head. In our study, the lock slopes at 16% show those features, and the effect is not only occurring within the inclined lock but is also observed in the downstream flat part of the channel.

#### 4.2 Ambient fluid entrainment

Kelvin–Helmholtz instabilities have a major role in provoking water entrainment. They take the form of vortical movements generated due to velocity shear at the interface between the two fluids. Since shear stress is determinant in the process of water entrainment, a new quantity to account for the potential entrainment capacity of the gravity current is defined here on the basis of the computed time evolution of the interfacial shear stress ( $\tau_m$ ). It is computed as the nondimen-

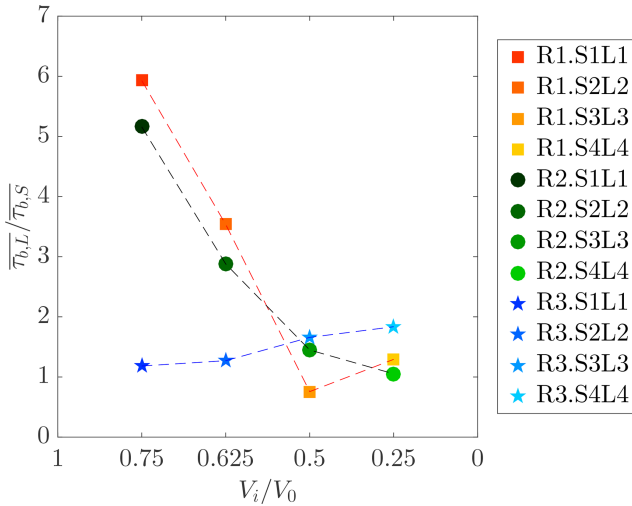


**Figure 6.** Ratio between time-averaged bed shear stress of tests with varying lock lengths ( $\overline{\tau_{b,L}}$ ) and test with varying lock slopes ( $\overline{\tau_{b,S}}$ ) versus percentage of volume of the upstream lock reach  $V_i/V_0$ . Dashed lines link tests performed with the same initial excess density.

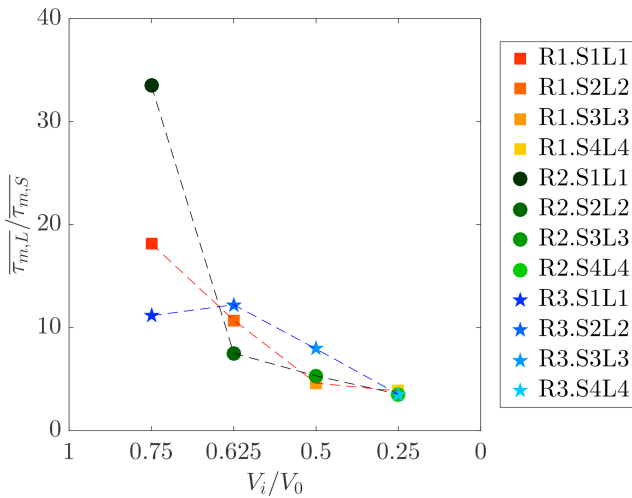


**Figure 7.** Ratio between time-averaged interface shear stress of tests with varying lock lengths ( $\overline{\tau_{m,L}}$ ) and test with varying lock slopes ( $\overline{\tau_{m,S}}$ ) versus percentage of volume of the upstream lock reach  $V_i/V_0$ . Dashed lines link tests performed with the same initial excess density.

sional time integral of the shear stress that represents, after dimensional analysis, the work done over a determined duration per unit surface for a given advection velocity, which can be approximated as the initial buoyancy velocity,  $u_0$ . This quantity  $\Phi_m$  is calculated as

$$\Phi_m = \int_{T_1}^{T_2} \tau_m(t) dt / t^*, \quad (10)$$

where the limits of integration are  $T_1 = L_h$  and  $T_2 = L_b$  in order to focus on the body, the region that has been found to be most affected by the variation of the initial conditions. The validity of the use of  $\Phi_m$  as an indicator of the entrainment capacity is supported by the analysis of its relation with the Richardson number  $Ri$  (Zordan et al., 2018b). The relation between water entrainment and bulk Richardson number is well known in the literature and numerous empirical fits to the experimental data have been proposed since the early work of Parker et al. (1987) and supported by the more recent contributions of Stagnaro and Pittaluga (2014). Since bulk Richardson number is based on depth-averaged quantities, it assumes that properties do not vary significantly along the vertical. The quantity  $\Phi_m$ , a surrogate for entrainment capacity, relies on instantaneous measurements of shear stress and therefore accounts for the unsteady behavior of the currents. Therefore, it is proposed here to use this quantity as a surrogate for water entrainment capacity since it benefits from instantaneous measurements of shear stress and it accounts for the unsteady behavior of the gravity currents. In Fig. 11, the potential water entrainments for gravity currents performed on an incline and correspondent tests with a reduced initial volume of release are compared. The tests  $R_i.S4$  and  $R_i.L4$  detach from the identity line, and thus a greater water entrainment is expected for the case with the inclined bed with respect to the horizontal bottom. The enhanced entrainment that has been verified for gravity currents formed downstream of steep slopes is due to the shear at the interface with the ambient water. According to Beghin et al. (1981), gravity currents are experiencing two phases while flowing along the channel. An initial acceleration takes place due to higher gravitational forces, and then the current accelerates, inducing an increment of shear stresses at the interface. The entrainment of clear water is therefore intensified and the currents are diluted. At the point at which the measurements are taken, the gravity currents are experiencing this second phase.

### 4.3 Bottom erosion capacity

The magnitude of the shear stress at the lower boundary layer determines the sediment transport capacity of saline currents and whether erosion or deposition processes dominate the regime at the bottom boundary (Cossu and Wells, 2012). Therefore, similarly to the interfacial water entrainment capacity, the bottom entrainment capacity, which can also be called the erosion capacity, is computed here on the basis of the computed bed shear stress.

This new quantity is defined as

$$\Phi_b = \int_{T_1}^{T_2} \tau_b(t) dt / t^*, \quad (11)$$

where the limits  $T_i$  are  $T_1 = 0$  and  $T_2 = L_b$ .

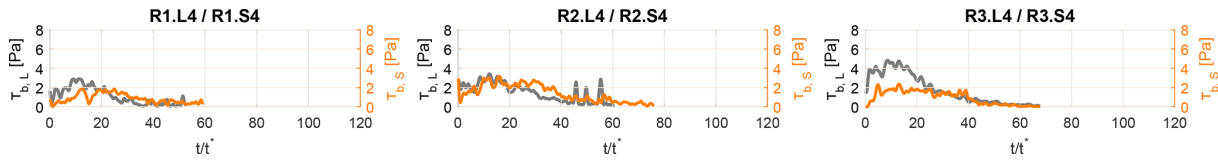


**Figure 8.** Temporal evolution of bed shear stresses calculated by log-law fitting for tests with progressively reduced lock length ( $\tau_{b,L}$ ) and with the lock slope ( $\tau_{b,S}$ ).

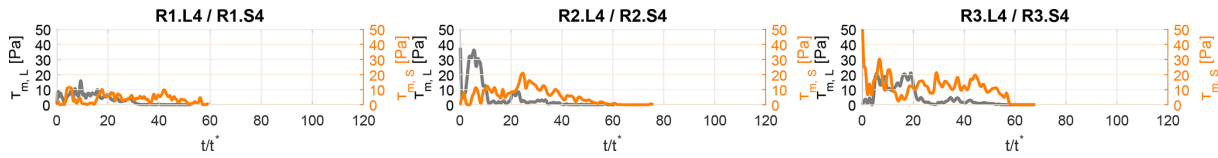


**Figure 9.** Temporal evolution of interfacial shear stresses calculated by log-law fitting for tests with progressively reduced lock length ( $\tau_{m,L}$ ) and with the lock slope ( $\tau_{m,S}$ ).

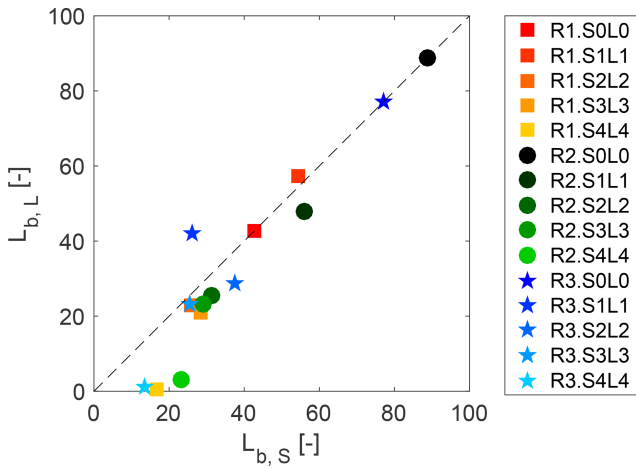


**Figure 10.** Comparison of the length of the body ( $L_b$ ) between tests with progressively reduced lock length and with lock slope. The dashed line is the identity line.

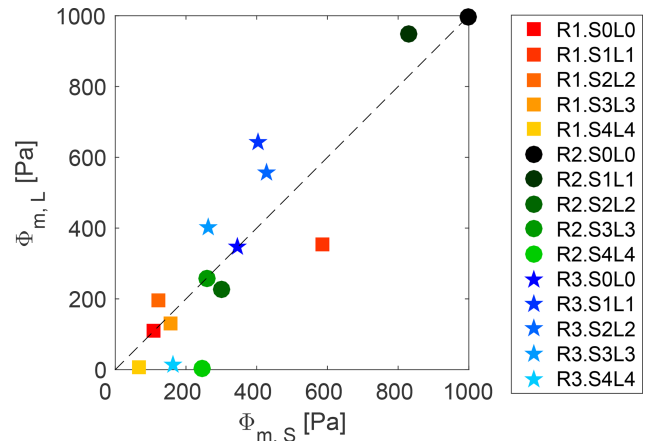


**Figure 11.** Comparison of  $\Phi_m$ , a surrogate for the entrainment capacity of the mixing region, between tests with lock slope ( $S_i$ ) and correspondent tests on a horizontal bottom ( $L_i$ ). The dashed line is the identity line.

In Zordan et al. (2018a) this quantity has been estimated for gravity currents simulated over an erodible bed. A relationship between the eroded volume of sediments provoked by the passage of the gravity current and  $\Phi_b$  has been found, therefore confirming that  $\Phi_b$  is a good estimator of the entrainment capacity of these flows. Although the present experiments are over a fixed bed, this estimator will be used here to evaluate the influence of the lock initial conditions on the entrainment capacity of these flows.

The bottom erosion capacity is compared for gravity currents performed with the lock slope and correspondent tests on a horizontal bottom. Generally,  $L_i$  tests show a higher erosion capacity with respect to their analogous  $S_i$ . The points in Fig. 12 are in fact concentrated above the bisect of the first and third quadrants. The effect of an extra gravitational force occurring in the flow upstream of the lock, as described above, is proven not to play a role in enhancing the capacity

of the current to perform bottom erosion in the downstream flat reach of the channel, which is instead reduced. This is probably a consequence of the decrease in streamwise velocity that results from the dilution of the gravity current already occurring in the lock. On the other hand, ambient water entrainment causes the expansion of the body region. Longer bodies keep eroding material longer, and the erosion potential attributed to this part is therefore increasing. The potential bottom erosion, i.e., the quantity  $\Phi_b$  in Fig. 13, shows a tendency to decrease with increasing lock slope. This is mainly the result of the released volume reduction caused by the presence of the lock slope, therefore originating shorter current bodies. The role of the body in the total erosion capacity is computed as the ratio  $\Phi_{b-body}/\Phi_b$  (Fig. 13), whose limits of integration of  $\Phi_{b-body}$  are  $T_1 = L_h$  and  $T_2 = L_b$ . The contribution that is ascribed to the body has a similar devel-

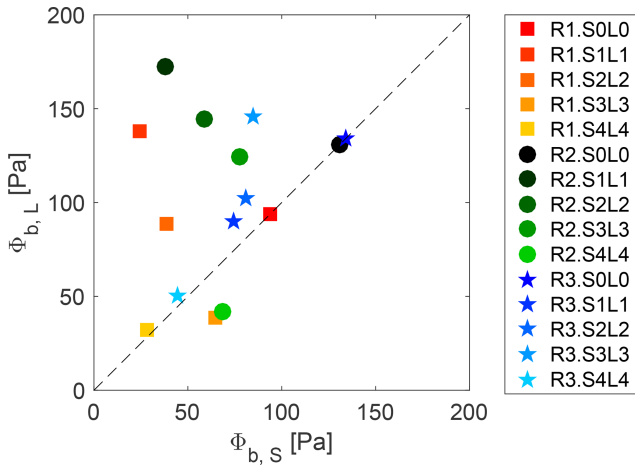


**Figure 12.** Comparison of the bottom erosion capacity  $\Phi_b$  between tests with lock slope ( $S_i$ ) and correspondent tests on a horizontal bottom ( $L_i$ ). The dashed line is the identity line.

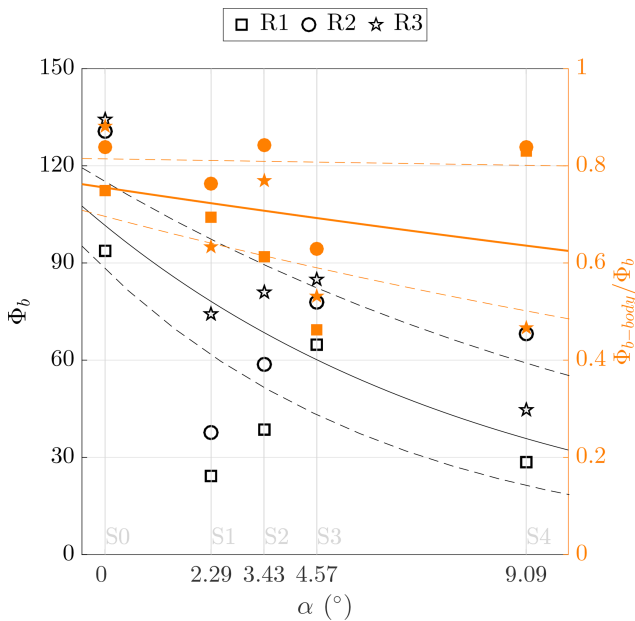


**Figure 13.** Potential erosion capacity for gravity currents (left axis) developed with different lock inclinations and rate of potential bottom erosion due to the body of the gravity current on the total bottom erosion capacity,  $\Phi_{b-body}/\Phi_b$  (right axis). The exponential fitting lines are reported in order to give evidence of the general trend, together with the 85% confidence intervals (dashed lines).

opment as the total erosion capacity. This reinforces the hypothesis that the body is determinant in the entrainment capacity of a gravity current. Figure 13 highlights the fact that the importance of the body in the total erosion capacity becomes proportionally higher for tests S4 (the trend lines in Fig. 13 deviate more in this configuration). Higher water entrainment was proven in Sect. 4.2 for this latter case, which was therefore subjected to an expansion of the body region.

An influence of the upper surface on the dynamics of the lower bottom boundary is therefore hypothesized. The interaction between the upper layer and the bottom was already pointed out by the numerical investigation of Cantero et al. (2008), and experimental evidence was reported in Zordan et al. (2018b). In the latter, vorticity was analyzed, showing that residual negative vorticity expands from the upper layer through the bottom with progressively lower intensity.

### 5 Conclusions

In most practical situations gravity currents flow on different topographies and most of the time travel along inclined but discontinuous slopes (slope breaks). Moreover, they are generally originated by the release of a certain amount of a fluid of various densities. The present study analyzes all the previously mentioned changing initial conditions that trigger the gravity currents commonly observed in nature.

Gravity currents of different initial densities are reproduced experimentally and the effect of incremental gravitational forces (reproduced by using an inclined lock) is analyzed. Corresponding tests with a horizontal lock are performed as well in order to have reference cases with the same reduced volume. The range of lock slopes tested varies from a horizontal bed to  $S = 16\%$  (which corresponds to an inclination of the lock  $\alpha \approx 9^\circ$ ). The gravitational force is the main driving force that directly depends on slope (Khavasi et al., 2012). Therefore, at the upstream inclined reach that constitutes the lock, there is an action of gravitational forces that competes with the entrainment that takes place due to higher shear stress at the upper interface and tends to dilute the current. Thus, if, on the one hand, gravitational acceleration drives a faster gravity current, water entrainment at the upper interface, on the other hand, dilutes the fluid of the current that is consequently slowed down and expands due to the incorporation of the ambient fluid. The configurations S4 and L4, corresponding to the steepest lock slope and the shortest lock length, respectively, exhibit the highest deviations in terms of shape and ambient water entrainment between tests with lock slopes with respect to correspondent tests on the horizontal bed. S4 tests showed a longer body owing to entrainment of the ambient fluid. Bottom erosion capacity at the downstream flat reach is reduced by the presence of the extra gravitational forces, most probably due to lower streamwise velocities that are a consequence of gravity current dilution occurring on the way of the gravity current along the channel. The limit case of tests S4, with a lock slope of  $S = 16\%$ , is the transient condition as described by previous literature for a continuously sloped channel (Britter and Linden, 1980; Beghin et al., 1981; Parker et al., 1987; Maxworthy and Nokes, 2007; Maxworthy, 2010) for which buoyancy force is large enough to counteract bottom and upper-layer frictions. The limit given by the experimental setup did not allow for

steeper lock slopes, and these are cases for which further investigation should therefore be undertaken.

**Data availability.** The datasets generated and/or analyzed during the current study are available from the corresponding author on reasonable request.

## Appendix A: List of symbols

Table A1 summarizes the list of symbols used in the paper, their definition and unit of measure.

**Table A1.** List of symbols with definition and unit of measure.

Symbol	Definition	Units
$A, B$	coefficients of the log fit	–
$g'$	reduced gravity	$\text{m s}^{-2}$
$h_0$	total height of the water column	m
$h_b$	vertical geometry scale	m
$h_{S_i}$	vertical elevation of the inclined bottom	m
$h(t)$	current height	m
$H(t)$	kinematic function	$\text{m s}^{-2}$
$k$	von Kármán constant	–
$k_s$	skin roughness	mm
$L_b$	temporal length of the body	s
$L_h$	temporal length of the head	s
$L$	lock length	m
$L_i$	test performed with lock length $i$	–
$n$	total number of observation	–
$R$	correlation coefficient	–
$R_i$	test performed with initial density $\rho_i$	–
$Re_0$	Reynolds number based on initial quantities	–
SSR	sum of square of the regression	–
TSS	total sum of square	–
$S$	slope	%
$S_i$	test performed with slope $i$	–
$t^*$	normalized timescale	–
$u$	instantaneous streamwise velocity	$\text{m s}^{-1}$
$u_*$	friction velocity	$\text{m s}^{-1}$
$\bar{u}$	mean streamwise velocity	$\text{m s}^{-1}$
$u'$	streamwise turbulent fluctuation	$\text{m s}^{-1}$
$u_0$	initial buoyancy velocity	$\text{m s}^{-1}$
$u_b$	buoyancy velocity	$\text{m s}^{-1}$
$u_d$	depth-averaged streamwise velocity	$\text{m s}^{-1}$
$V_i$	initial volume of dense fluid released	$\text{m}^{-3}$
$w$	instantaneous vertical velocity	$\text{m s}^{-1}$
$\bar{w}$	mean vertical velocity	$\text{m s}^{-1}$
$w'$	vertical turbulent fluctuation	$\text{m s}^{-1}$
$y_i$	response of the observation $i$	–
$\bar{y}_i$	average of the response of the observation $i$	–
$\hat{y}_i$	regression line of the response of the observation $i$	–
$z_0$	zero velocity level	m
$\alpha$	angle of inclination of the bottom	°
$\nu$	kinematic viscosity	$\text{m}^2 \text{s}^{-1}$
$\Phi_b$	bottom entrainment capacity	–
$\Phi_m$	interface entrainment capacity	–
$\Phi_{b\text{-body}}$	bottom entrainment capacity due to the body	–
$\rho_0$	gravity current initial density	$\text{g m}^{-3}$
$\rho_a$	ambient fluid density	$\text{kg m}^{-3}$
$\tau_b$	bed shear stress	Pa
$\tau_m$	interface shear stress	Pa

**Competing interests.** The authors declare that they have no conflict of interest.

**Acknowledgements.** This research was funded by the European project SEDITRANS funded by Marie Curie Actions, FP7-PEOPLE-2013-ITN-607394 (Multi-Partner Initial Training Networks).

**Review statement.** This paper was edited by Douglas Jerolmack and reviewed by Jorris Eggenhuisen, Chris Stevenson, and one anonymous referee.

## References

- Ancey, C.: Gravity flow on steep slope, vol. Buoyancy Driven Flows, Cambridge University Press New York, 2012.
- Azpiroz-Zabala, M., Cartigny, M. J., Talling, P. J., Parsons, D. R., Sumner, E. J., Clare, M. A., Simmons, S. M., Cooper, C., and Pope, E. L.: Newly recognized turbidity current structure can explain prolonged flushing of submarine canyons, *Sci. Adv.*, 3, e1700200, <https://doi.org/10.1126/sciadv.1700200>, 2017.
- Baas, J. H., McCaffrey, W. D., Haughton, P. D., and Choux, C.: Coupling between suspended sediment distribution and turbulence structure in a laboratory turbidity current, *J. Geophys. Res.-Oceans*, 110, 2005, <https://doi.org/10.1029/2004JC002668>, 2005.
- Beghin, P., Hopfinger, E., and Britter, R.: Gravitational convection from instantaneous sources on inclined boundaries, *J. Fluid Mech.*, 107, 407–422, 1981.
- Britter, R. and Linden, P.: The motion of the front of a gravity current travelling down an incline, *J. Fluid Mech.*, 99, 531–543, 1980.
- Cantero, M. I., Balachandar, S., García, M. H., and Bock, D.: Turbulent structures in planar gravity currents and their influence on the flow dynamics, *J. Geophys. Res.-Oceans*, 113, 2008, <https://doi.org/10.1029/2007JC004645>, 2008.
- Chassaing, P.: Mécanique des fluides, Cepadues éditions, 3eme édition, 554 pp., ISBN13 978-2-85428-929-9, 2010.
- Cossu, R. and Wells, M. G.: A comparison of the shear stress distribution in the bottom boundary layer of experimental density and turbidity currents, *Eur. J. Mech. B-Fluid.*, 32, 70–79, <https://doi.org/10.1016/j.euromechflu.2011.09.006>, 2012.
- Csanady, G. T.: Turbulent interface layers, *J. Geophys. Res.-Oceans*, 83, 2329–2342, 1978.
- Ellison, T. and Turner, J.: Turbulent entrainment in stratified flows, *J. Fluid Mech.*, 6, 423–448, 1959.
- Fer, I., Lemmin, U., and Thorpe, S.: Winter cascading of cold water in Lake Geneva, *J. Geophys. Res.-Oceans*, 107, 13-1–13-16, <https://doi.org/10.1029/2001JC000828>, 2002.
- Ferreira, R. M.: The von Kármán constant for flows over rough mobile beds. Lessons learned from dimensional analysis and similarity, *Adv. Water Resour.*, 81, 19–32, 2015.
- Ferreira, R. M., Franca, M. J., Leal, J. G., and Cardoso, A. H.: Flow over rough mobile beds: Friction factor and vertical distribution of the longitudinal mean velocity, *Water Resour. Res.*, 48, <https://doi.org/10.1029/2011WR011126>, 2012.
- Franca, M. and Lemmin, U.: Eliminating velocity aliasing in acoustic Doppler velocity profiler data, *Meas. Sci. Technol.*, 17, 313, <https://doi.org/10.1088/0957-0233/17/2/012>, 2006.
- Goring, D. G. and Nikora, V. I.: Despiking acoustic Doppler velocimeter data, *J. Hydraul. Eng.*, 128, 117–126, 2002.
- Huppert, H. E.: Gravity currents: a personal perspective, *J. Fluid Mech.*, 554, 299–322, 2006.
- Hurth, D. and Lemmin, U.: A correction method for turbulence measurements with a 3D acoustic Doppler velocity profiler, *J. Atmos. Ocean. Tech.*, 18, 446–458, 2001.
- Khavasi, E., Afshin, H., and Firoozabadi, B.: Effect of selected parameters on the depositional behaviour of turbidity currents, *J. Hydraul. Res.*, 50, 60–69, 2012.
- Kneller, B. and Buckee, C.: The structure and fluid mechanics of turbidity currents: a review of some recent studies and their geological implications, *Sedimentology*, 47, 62–94, 2000.
- Lemmin, U. and Rolland, T.: Acoustic velocity profiler for laboratory and field studies, *J. Hydraul. Eng.*, 123, 1089–1098, 1997.
- Lofquist, K.: Flow and stress near an interface between stratified liquids, *Phys. Fluids*, 3, 158–175, 1960.
- Maxworthy, T.: Experiments on gravity currents propagating down slopes. Part 2. The evolution of a fixed volume of fluid released from closed locks into a long, open channel, *J. Fluid Mech.*, 647, 27–51, 2010.
- Maxworthy, T. and Nokes, R.: Experiments on gravity currents propagating down slopes. Part 1. The release of a fixed volume of heavy fluid from an enclosed lock into an open channel, *J. Fluid Mech.*, 584, 433–453, 2007.
- Mulder, T. and Alexander, J.: Abrupt change in slope causes variation in the deposit thickness of concentrated particle-driven density currents, *Mar. Geol.*, 175, 221–235, 2001.
- Nezu, I., Nakagawa, H., and Jirka, G. H.: Turbulence in open-channel flows, *J. Hydraul. Eng.*, 120, 1235–1237, 1994.
- Niño, Y. and Garcia, M.: Experiments on particle-turbulence interactions in the near-wall region of an open channel flow: implications for sediment transport, *J. Fluid Mech.*, 326, 285–319, 1996.
- Nogueira, H. I., Adduce, C., Alves, E., and Franca, M. J.: Dynamics of the head of gravity currents, *Environ. Fluid Mech.*, 14, 519–540, 2014.
- Palmieri, A., Shah, F., and Dinar, A.: Economics of reservoir sedimentation and sustainable management of dams, *J. Environ. Manage.*, 61, 149–163, 2001.
- Parker, G., Garcia, M., Fukushima, Y., and Yu, W.: Experiments on turbidity currents over an erodible bed, *J. Hydraul. Res.*, 25, 123–147, 1987.
- Salim, S., Pattiaratchi, C., Tinoco, R., Coco, G., Hetzel, Y., Wijeratne, S., and Jayaratne, R.: The influence of turbulent bursting on sediment resuspension under unidirectional currents, *Earth Surf. Dynam.*, 5, 399–415, <https://doi.org/10.5194/esurf-5-399-2017>, 2017.
- Schleiss, A. J., Franca, M. J., Juez, C., and De Cesare, G.: Reservoir sedimentation, *J. Hydraul. Res.*, 54, 595–614, 2016.
- Simpson, J. E.: Effects of the lower boundary on the head of a gravity current, *J. Fluid Mech.*, 53, 759–768, 1972.
- Simpson, J. E.: Gravity currents: In the environment and the laboratory, Cambridge university press, 1997.
- Stagnaro, M. and Bolla Pittaluga, M.: Velocity and concentration profiles of saline and turbidity currents flowing in a straight chan-

- nel under quasi-uniform conditions, *Earth Surf. Dynam.*, 2, 167–180, <https://doi.org/10.5194/esurf-2-167-2014>, 2014.
- Traer, M., Hilley, G., Fildani, A., and McHargue, T.: The sensitivity of turbidity currents to mass and momentum exchanges between these underflows and their surroundings, *J. Geophys. Res.-Earth*, 117, <https://doi.org/10.1029/2011JF001990>, 2012.
- Turner, J. S.: *Buoyancy effects in fluids*, Cambridge University Press, 1973.
- Ungarish, M.: *An introduction to gravity currents and intrusions*, CRC Press, 2009.
- Zordan, J., Schleiss, A. J., and Franca, M. J.: Bed shear stress estimation for gravity currents performed in laboratory, *Proc. of River Flow 2016*, St. Louis, USA, 855–861, 2016.
- Zordan, J., Juez, C., Schleiss, A. J., and Franca, M. J.: Entrainment, transport and deposition of sediment by saline gravity currents, *Adv. Water Resour.*, 115, 17–32, <https://doi.org/10.1016/j.advwatres.2018.02.017>, 2018a.
- Zordan, J., Schleiss, A. J., and Franca, M. J.: Structure of a dense release produced by varying initial conditions, *Environ. Fluid Mech.*, 2018b.